RSC Advances

PAPER

View Article Online
View Journal | View Issue

Cite this: *RSC Adv.*, 2026, **16**, 27960

Anchored dilacunary phosphotungstates on zeolite HY: synthesis and solvent free selective oxidation of levulinic acid to succinic acid using environmentally benign oxidant, H_2O_2

Margi Joshi and Anjali Patel *

The purpose of this research is to develop a highly efficient, atom-economical protocol for biomass valorization by targeting the challenging selective oxidation of levulinic acid into succinic acid. Addressing a long-standing challenge in biomass oxidation chemistry, this study outlines the design of an inorganic tungsten – oxygen rich dilacunary phosphotungstate anchored to zeolite HY, forming a redox-active heterogeneous catalyst. For the first time, complete selectivity toward succinic acid with a 42% yield was achieved using hydrogen peroxide as a green oxidant under mild, solvent-free conditions. The major innovation lies in utilizing the unique structural confinement and cooperative acidity of the faujasite supercages and phosphotungstates, which allowed the catalyst to significantly outperform the previously reported supports, opening new horizons towards dicarboxylic acid production. Comprehensive physicochemical characterization confirmed the successful incorporation of the active species and revealed the structural and acidic features responsible for catalytic performance. The reaction was carried out in a simple batch reactor, and systematic investigation of key reaction parameters enabled precise regulation of the reaction pathway, delivering a turnover number of 462. Mechanistic insights were gained through radical-scavenging and control experiments, elucidating the nature of the active oxidant and the reactive species involved. This highly controlled radical network precisely directs the oxidative cleavage at the C3–C4 bond of levulinic acid while completely suppressing over-oxidation pathways. The effectiveness of the developed system was highlighted through comparison with previously reported methods, and recycling experiments demonstrated catalyst stability up to 4 cycles. Overall, the developed methodology provides a blueprint for future inorganic materials design for the sustainable transformation of biomass-derived molecules into high-value chemical products.

Received 17th April 2026
Accepted 18th May 2026

DOI: 10.1039/d6ra03282f

rsc.li/rsc-advances

Introduction

Oxidation reactions form the backbone of numerous chemical transformations and play a central role in converting simple feedstocks into functionalized and value-added compounds. They are among the most studied yet challenging classes of reactions due to their intrinsic complexity involving multi-electron and proton transfer processes. The selectivity and efficiency of oxidation processes depend strongly on the interplay between the oxidant type and the catalyst design, which together dictate the activation pathway of oxygen and the stabilization of reactive intermediates.[1–8] In this regard, advanced heterogeneous architectures and engineered catalysts have emerged as vital tools for improving efficiency across various biomass valorization sectors.[9–11] Furthermore, alternative strategies utilizing structured mixed-metal oxides and stable solid-state frameworks have expanded the scope of sustainable redox transformations under diverse operational regimes.[12,13] For instance, the selective oxidation of levulinic acid to succinic acid remains a scarcely explored yet promising pathway in biomass valorization, particularly due to the challenge of achieving high product specificity under green and mild conditions. Oxidation of one of the most promising C5 bioplatforms, levulinic acid was explored through multiple pathways yielding a diverse array of value-added products (Fig. 1) depending on the reaction conditions, catalyst nature and selectivity mechanisms.[14] In the wider biorefinery landscape, transitioning from corrosive mineral acids to structured solid platforms remains a critical baseline for these upgrading strategies.[15] For instance, unconfined liquid-phase networks utilizing homogeneous manganese catalysts typically steer aerobic C–C cleavage portfolios toward mixed fatty acids,[16]

Polyoxometalates and Catalysis Laboratory, Department of Chemistry, Faculty of Science, The Maharaja Sayajirao University of Baroda, Vadodara 390020, Gujarat, India. E-mail: anjali.patel-chem@msubaroda.ac.in

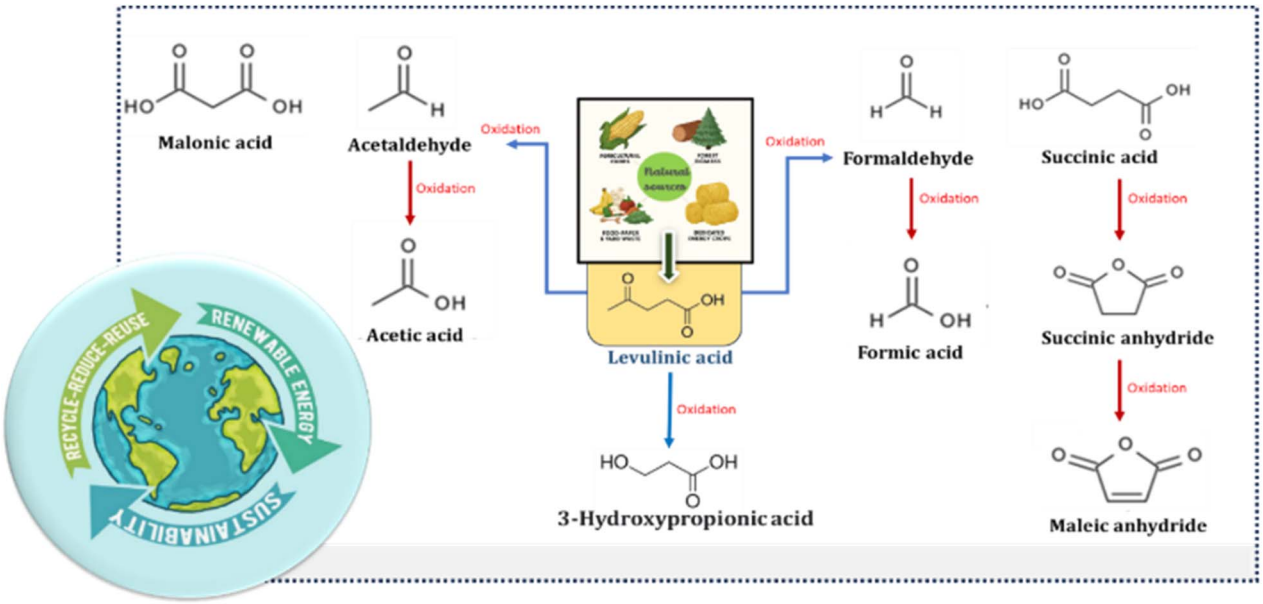

Fig. 1 Levulinic acid oxidation to different value-added products.

whereas ambient electrocatalytic setups drive the molecule toward valeric derivatives.[17] Alternatively, gas-phase operations over supported vanadates switch the selectivity entirely toward a terminal methyl-carbon scission to yield maleic anhydride instead of internal alkyl cleavage.[18] Detailed mechanistic and spectroscopic evaluations confirm that this vapor-phase pathway is governed by an initial intramolecular cyclization to lactone intermediates prior to forming the anhydride.[19]

Among the various routes, the conversion of levulinic acid to succinic acid has garnered significant interest, as succinic acid is a key renewable platform chemical with broad applications in biodegradable polymers, specialty chemicals, and green solvents, alongside increasing industrial demand for sustainable, bio-based materials.[20–25] The earliest attempt was carried out by Tollens in 1879, employing dilute nitric acid as the oxidant. Although the yield of succinic acid was modest, the reaction generated several low-molecular-weight carboxylic acids as by-products.[26] In contrast, a patent filed by A. P. Dunlop and co-workers in 1954 described a gas-phase oxidation route using molecular oxygen and a vanadium-based catalyst at 375 °C, achieving a succinic acid yield of up to 83%.[27] However, the practicality of this method was constrained by the harsh reaction conditions. Although initial efforts to produce succinic acid date back over a century, surprisingly few reports have emerged since, highlighting the persistent challenge and untapped potential in this area.[21,26,28,29] Podolean *et al.* (2013) reported the use of Ru nanoparticles supported on functionalized magnetic silica, exhibiting high oxidation activity with O_2 as the oxidant.[28] Likewise, Kawasumi *et al.* (2017) employed *in situ* generated *tert*-butyl hypoiodite (*t*-BuOI) from I_2 and *t*-BuOK as a selective oxidizing agent.[29] Carnevali *et al.* (2018) demonstrated the catalytic potential of tungstic acid (H_2WO_4) in the presence of H_2O_2,[21] while Arriaga-Arellano *et al.* (2024) reported Ru-based catalysts supported on Fe_2O_3, CeO_2, Al_2O_3, SiO_2, zeolites, and carbon[26] showing high efficiency and versatility in oxidative transformations using both O_2 and H_2O_2 as oxidants. The main key observations from the literature study are given below:

(I) The aspect of selective oxidation of levulinic acid to succinic acid is still a challenge.

(II) Despite its green nature, hydrogen peroxide remains less studied as an oxidant for levulinic acid conversion.

(III) Most reported systems still require organic solvents, indicating scope for developing solvent-free or aqueous catalytic systems. The use of highly recyclable, bio-based catalysts under solvent-free regimes represents a highly sustainable approach to address this challenge.[30]

(IV) No reports available on anchored polyoxometalates, despite being excellent candidates in the oxidation reactions.

Polyoxometalates (POMs) are highly effective oxidation catalysts due to their redox flexibility and ability to mediate reversible multi-electron transfer processes.[2,3,31–36] In particular, lacunary POMs possess coordinatively unsaturated metal sites arising from structural vacancies. The precise engineering of these vacancies and the systematic incorporation of active elements into the lacunary framework[37,38] enhance oxidant activation and facilitate peroxo intermediate formation. This structural versatility has led to their successful application across various efficient catalytic systems[39–41] enabling improved selectivity under mild oxidation conditions.

The choice of oxidant critically governs the course and selectivity of oxidation reactions. Hydrogen peroxide is considered a mild yet highly versatile oxygen donor. Its relatively weak O–O bond facilitates the generation of reactive peroxo species in the presence of suitable catalysts, enabling efficient oxidation under mild conditions. These peroxo intermediates selectively attack electron-rich functional groups such as carbonyls, alcohols, or C=C bonds without requiring elevated temperature or pressure. Moreover, the only byproduct of H_2O_2 decomposition

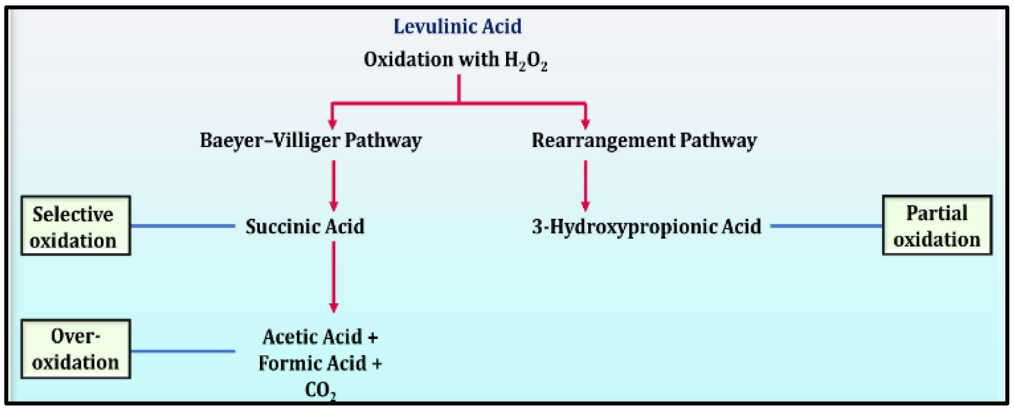

Fig. 2 Possible oxidation routes of levulinic acid with hydrogen peroxide.

is water, making it an environmentally benign and atom-efficient oxidant.[42–46] Compared with molecular oxygen, H_2O_2 exhibits superior solubility in aqueous media, easier activation, and greater control over selectivity,[14,21] particularly in Baeyer–Villiger-type oxidations and mild functional group transformations.[14,21,47–51] Fig. 2 schematically summarizes the possible oxidation routes and products obtained during the oxidation of levulinic acid with hydrogen peroxide. Interestingly, the formation of C4 succinic acid from C5 levulinic acid proceeds *via* C–C bond cleavage with the concomitant liberation of C1 species (CO_2/Formic acid).

The fundamental understanding of structure–activity relationships in lacunary polyoxometalate-based systems is more interesting. The incorporation of dilacunary phosphotungstate to a zeolitic framework introduces a unique inorganic interface where the redox-active tungsten centers, structural vacancies, and Brønsted acidity of the support act cooperatively (Fig. 3). Such integration is expected to not only stabilizes the lacunary architecture but also modulates its electronic environment, thereby influencing oxidant activation and intermediate stabilization pathways. In particular, the role of defect sites in facilitating selective oxygen transfer remains underexplored in heterogeneous systems. It provides insight into how rational design of polyoxometalates with available vacancy anchored on microporous supports can bridge the gap between homogeneous-like reactivity and heterogeneous stability, offering a promising direction for designing next-generation oxidation catalysts. In light of this, recently A. Patel and co-worker reported a bifunctional catalyst comprising lacunary POMs and zeolite Hβ, however its performance in esterification was comparatively better than oxidation[52] So, by taking different support may be the conversion rates can be increased.

The fundamental scientific hypothesis rests on creating a unique catalytic interface that coordinates high Brønsted acidity with highly accessible, localized redox centers under a restricted molecular geometry. We hypothesized that the framework of Zeolite HY could act as structural anchors for the open, electron-deficient oxygen vacancies found in dilacunary

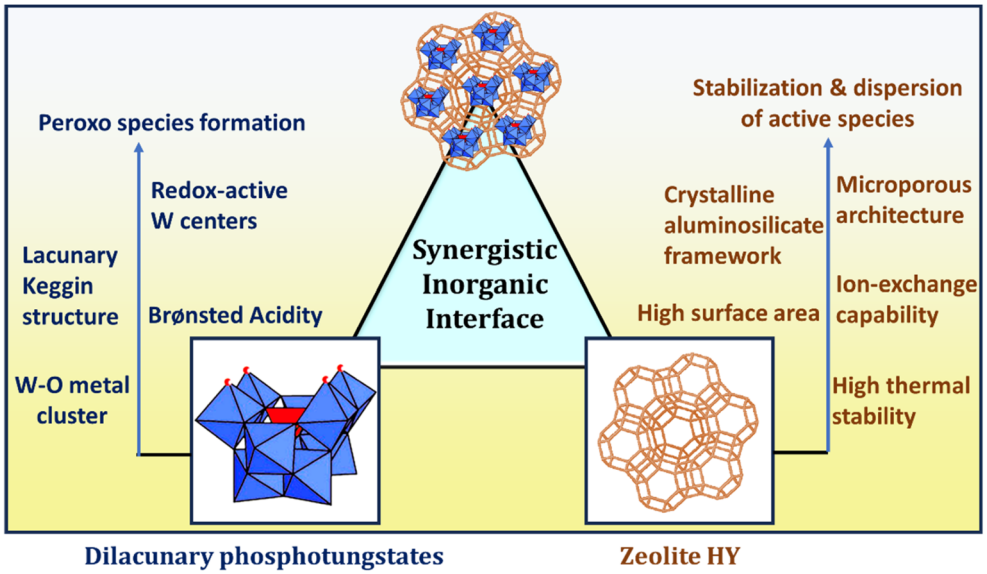

Fig. 3 Lacunary W–O cluster in zeolitic environment.

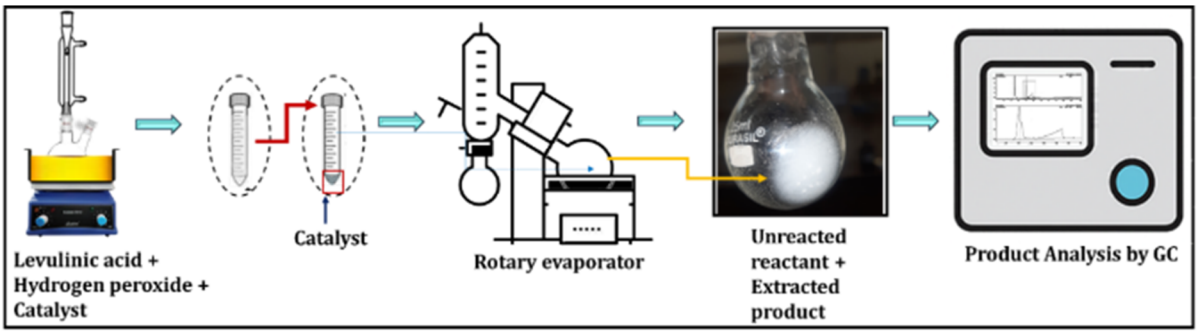

Scheme 1 Oxidation of levulinic acid.

clusters *via* surface silanol interactions. This strategic combination was hypothesized to achieve three critical goals: first, the restricted space (confinement effect) within the zeolite supercages would physically stabilize the active polyoxometalate phase against industrial leaching; second, the high concentration of surrounding Brønsted acid protons would actively accelerate the homolytic activation of hydrogen peroxide into highly active, surface-bound peroxo-tungsten radical species; and third, the strict spatial layout within the zeolite pores would direct the oxidation pathway exclusively toward the target C–C bond cleavage of levulinic acid, suppressing parallel, non-selective radical degradation pathways that form unwanted byproducts. Therefore, by tailoring this synergy, an exceptionally clean and reusable solvent-free transformation could be achieved.

In light of the present scenario, the urge to develop a catalyst capable of achieving maximum selectivity towards succinic acid has become increasingly important, especially one that is both redox-active and highly stable. With this motivation, a dilacunary phosphotungstate (PW_{10}) anchored to zeolite HY was considered for exploration. In this work, the synthesis and characterization of PW_{10}/ZHY are discussed, followed by its application in the synthesis of succinic acid through the relatively less explored oxidation pathway. The role of the oxidant and the contribution of each catalytic component were understood through control and scavenger experiments. The ability of the catalyst to sustain its activity across multiple recycling runs was also evaluated. Finally, the core idea of the present work is highlighted through a comparative study, supported by the proposed reaction mechanism.

Experimental

Materials

All chemicals used were of A.R. grade. Disodium hydrogen phosphate (≥99%), sodium tungstate dihydrate (≥99%), 30% hydrogen peroxide, levulinic acid (98%), succinic acid (≥99%), isopropyl alcohol (≥99.5%), *tert*-Butyl alcohol (≥99.5%) were used as received from Merck. zeolite NaY was purchased commercially from Reliance Industries Limited.

Synthesis of catalyst

The series of PW_{10} anchored zeolite HY catalysts was prepared in three steps: (i) synthesis of dilacunary phosphotungstates (ii) conversion of zeolite NaY to protonic form (ZHY), and (iii) anchoring of PW_{10} to ZHY *via* wet impregnation method and the resulting material was designated as PW_{10}/ZHY. Detailed procedures are provided in the SI.

Leaching test

The catalyst was suspended in water for 24 hours and then treated with ascorbic acid,[53] which gives no blue coloration, indicating no leaching of PW_{10} from ZHY.

Characterization

The PW_{10} loading on ZHY was varied between 10 and 40 wt%, and the catalyst containing 30 wt% PW_{10} demonstrated the highest acidity and catalytic efficiency, therefore, it was selected. The detailed characterization of PW_{10}/ZHY can be find in our previous publication.[54] However, here acidity measurements, FTIR, TGA, BET, XRD and HRTEM were discussed for the reader's convenience along with the additional new characterization such as NH_3-TPD, EDS and ^{29}Si MAS NMR.

Catalytic activity

The oxidation of levulinic acid with hydrogen peroxide was carried out and the detailed procedure is given in the SI. The schematic presentation for the same is given in Scheme 1.

Results and discussions

Characterization

The results of acidity obtained *via* titration methods are discussed here (Fig. 4).

Potentiometric and *n*-butyl amine titrations were performed to explicitly determine the shifts in acid strength and quantify the accumulation of newly introduced active protons on the material. ZHY possess acidic strength of 289 mV along with 0.8 (0.4 very strong + 0.4 strong) mEq g^{-1} strong acidic sites, with a total acidity of 0.83 mmol g^{-1}. After anchoring with phosphotungstates, the acidity of zeolite was increased and which is reflected in terms of acidic strength (400 mV), strong acidic sites (very strong = 2.3 mEq g^{-1}, strong = 1.5 mEq g^{-1}) as well as total acidity (1.10 mmol g^{-1}). This rise in acidity is mainly concerned with the Brønsted acidity, introduced *via* PW_{10}.

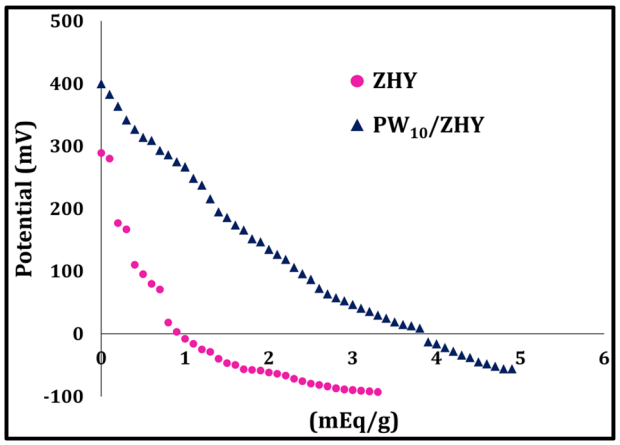

Fig. 4 Potentiometric titration curves.

Hence, from both *n*-butyl amine and potentiometric titration methods, the increment in total acidity was concluded.

While these independent titration pathways provide clear verification of enhanced active proton density, they do not establish the definitive elemental layout responsible for this change. To quantitatively confirm that this acidity corresponds to the stoichiometric incorporation of the target hetero polyanion species, the investigation transitions directly to chemical composition analysis through elemental measurements.

The results obtained *via* elemental analysis are presented in Table 1 and Fig. 5. It was conducted to quantitatively confirm that the intended stoichiometric elemental ratios of phosphorus and tungsten were successfully embedded into the composite matrix. It was found that, the theoretically calculated values are quite good agreement with the EDX values, which indicates effective impregnation of PW_{10} within zeolite. Further, these results were correlated with the ICP analysis. The obtained wt% of P (0.21%) and W (14.53%) are in good accordance, which confirmed the absence of leaching.

Further, these results were correlated with the NH_3-TPD analysis. This action was executed because ammonia acts as a highly selective probe molecule capable of penetrating the crystalline channels to thermally resolve and map out the distribution of distinct weak, moderate, and strong acid sites. NH_3-TPD profiles of ZHY and PW_{10}/ZHY are given in Fig. 6. ZHY possess a broad desorption envelope corresponding to two desorption peaks corresponds to weak and moderate acidic sites, mainly in the temperature range of 180–210 °C and 300–350 °C respectively with the acidity values 0.370 mmol g^{-1} and 0.230 mmol g^{-1}. From these data, the total acidity was found to be 0.60 mmol g^{-1}. The nature of profile as well as obtained

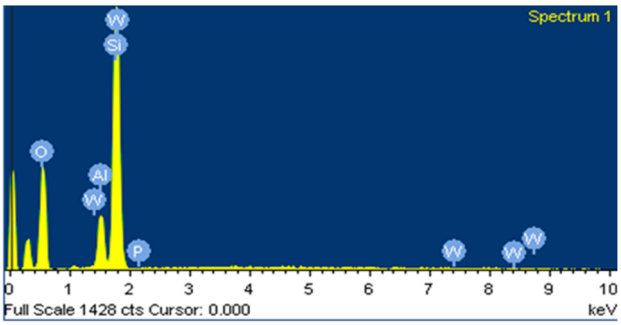

Fig. 5 EDS of PW_{10}/ZHY.

values are in a good accordance with the available literature.[55] PW_{10}/ZHY displays a continuous distribution of acid strength with three recognizable desorption regions three distinct desorption peaks due to weak (0.15 mmol g^{-1}), moderate (0.43 mmol g^{-1}) and strong acidic sites (0.52 mmol g^{-1}) appearing at approximately 203 °C, 405 °C and 620 °C, respectively. From which, the total acidity was determined to be 1.10 mmol g^{-1}. The broad and overlapping nature of these signals indicates a complex range of acidic environments resulting from the interaction between dilacunary species and the zeolite framework.

While comparing both profiles, it is clearly observed that the acidity of catalyst is significantly higher than that of support, which is due to the presence of dilacunary phosphotungstates which are rich in Brønsted acidity. Also, the observed acidity trends are reliable with the findings obtained by potentiometric titration and *n*-butylamine titration measurements.

BET surface area measurements of PW_{10}/ZHY exhibited lower surface area (200 m^2 g^{-1}) and pore volume (0.015 cm^3 g^{-1}) than that of ZHY (560 m^2 g^{-1}, 0.034 cm^3 g^{-1}). This gas physisorption profiling was performed to capture the structural variations in physical surface area and pore restrictions, validating whether the active polyoxometalate molecules inside the composite are successfully accommodated within the available host framework void spaces. The observed decrease after PW_{10} incorporation in the textural properties suggests its successful anchoring inside the zeolite pores of support. Further, this can be also explained *via* nitrogen adsorption–desorption isotherms of PW_{10}/ZHY, that possess type I with H1 hysteresis loop, a characteristic of microporous materials with uniform pore structure, which is similar to that of observed for ZHY.[56] Hence, it indicates the intactness of zeolite structure even after anchoring and showcasing effective pore-filling inside the support.

It is to be noted that, while the PW_{10} cluster (~1.0 nm) is larger than the 12-membered ring window of ZHY (0.74 nm), the

Table 1 Elemental analysis of PW_{10}/ZHY

				P (wt%)		W (wt%)	
Material	Si (wt%)	O (wt%)	Al (wt%)	By EDX	Theoretical	By EDX	Theoretical
PW_{10}/ZHY	21.24	56.56	7.41	0.22	0.24	14.57	14.63

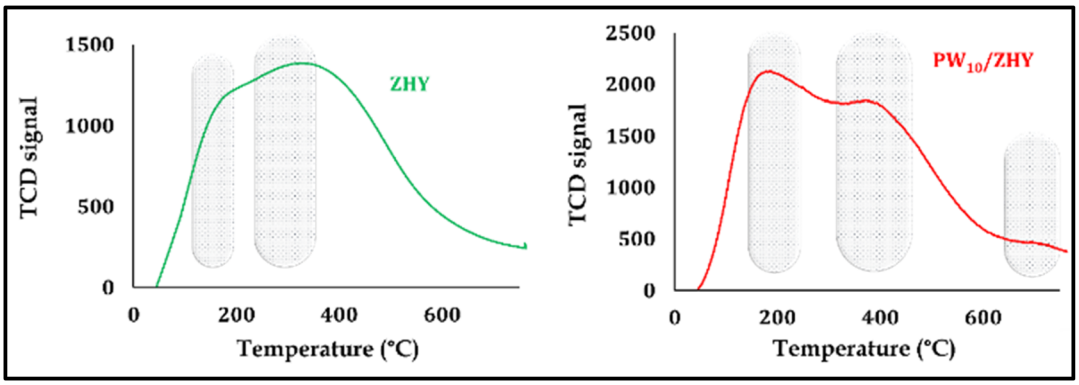

Fig. 6 NH_3-TPD profiles.

internal supercages (~1.3 nm) are sufficiently large to accommodate the Keggin units. The significant reduction in BET surface area and pore volume suggests that the PW_{10} clusters are likely anchored at the pore-mouths or within the accessible supercages near the crystal surface. This 'confinement effect' stabilizes the PW_{10} against leaching.

Further, the thermal stability of PW_{10}/ZHY was studied by TGA which is given in Fig. 7. This linear thermal degradation scanning was monitored to establish the safe operational temperature limits of the framework and to observe the exact temperatures at which structural collapse or polyanion breakdown takes place. In which, the total weight loss was observed mainly in two steps. As visible in from the profile, first weight loss subjected to loss of adsorbed water molecules and the second one is corresponded to the water of crystallization, giving a total weight loss of 25%. Afterwards, the catalyst was found to be stable up to 550 °C, confirming its high thermal stability. This high degree of thermal robustness strongly implies that the frameworks are held together by substantial chemical binding modes rather than weak physisorption overlayers. To clearly identify these specific molecular fingerprints and confirm that the primary lacunary Keggin geometry survives this robust interaction intact, Fourier transform infrared (FT-IR) spectroscopy was scrutinized.

FT-IR of PW_{10} shows the main characteristic peaks of P–O, W═O and W–O–W stretching at (1056, 1013 cm^{-1}), (964 cm^{-1}) and (888, 808 cm^{-1}) respectively, which shows the formation of di lacunary structure.[57] This infrared screening was analyzed to map out specific molecular finger-print framework vibrations, confirming that the chemical configuration of the active di-lacunary species remains intact. Further, FT-IR of PW_{10}/ZHY shows that the characteristic bands of PW_{10} are observed at 801 cm^{-1} (W–O–W), 960 cm^{-1} (W═O) and 1018 cm^{-1} (P–O), as presented in Fig. 8. The presence of these bands evidences the intact structure of PW_{10} after anchoring with that of ZHY. Also, the peaks at 463 cm^{-1} due to O–Si–O and O–Al–O bending, 570 cm^{-1} corresponds to ring vibration, 1059 cm^{-1} (Si–O–Si) and 1634 cm^{-1} (H–O–H bending) are the characteristic peaks of ZHY[56] that reflects the unaffected FAU structure of zeolite (SI Fig. 1). Interestingly, it the catalyst, significant shift in the peak values was observed that strongly reveals the interaction between terminal oxygen of dilacunary phosphotungstate and surface silanol groups of zeolite support.

To conclusively validate this silanol interaction at an atomic scale and trace the precise electronic environment modifications within the local silicon coordination shells, solid-state ^{29}Si MAS NMR measurements were systematically executed to understand the chemical environment of silicon before and after anchoring, ^{29}Si MAS NMR was studied.

This solid-state nuclear magnetic resonance measurement was conducted to track precise coordination environment shifts

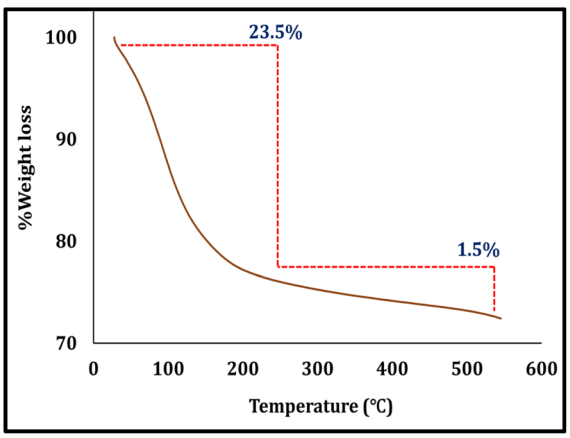

Fig. 7 TGA of PW_{10}/ZHY.

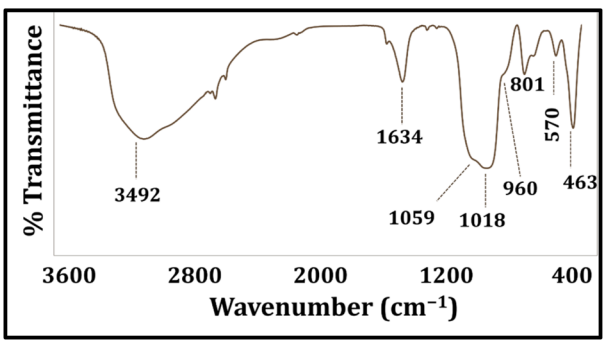

Fig. 8 FT-IR spectra of PW_{10}/ZHY.

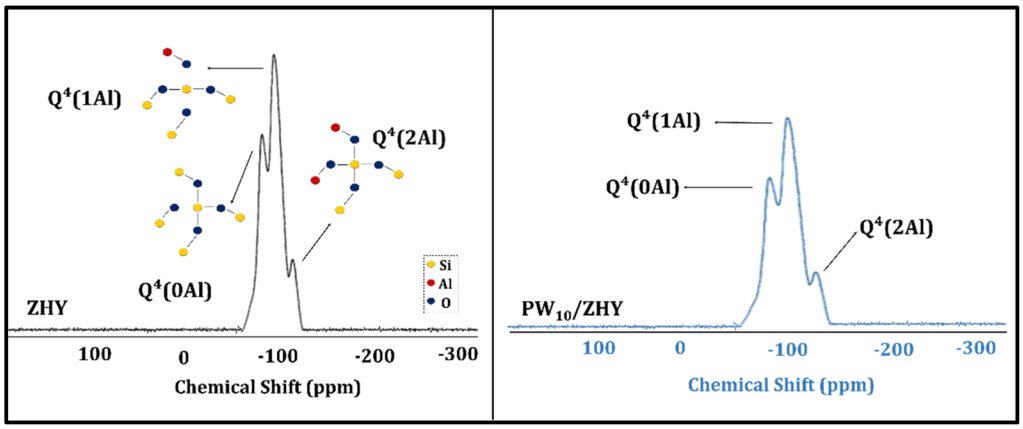

Fig. 9 ^{29}Si NMR spectra.

within the silicate framework, validating if the cluster is bound *via* local silanol defects without causing widespread disruption to the crystalline host network. The spectra of ZHY (Fig. 9) exhibited three different types of silicon nuclei Q^4(0Al), Q^4(1Al) and Q^4(2Al) with chemical shift values at −95, −101 and −107 ppm respectively. These values are in a good accordance with the reported literature, assuring the well-crystallized zeolite framework.[58] Likewise, PW_{10}/ZHY exhibits three different silicon nuclei corresponding to Q^4 (0Al) at −95.6 ppm, Q^4 (1Al) at −102 ppm and Q^4 (2Al) at −107.9 ppm. These silicon nuclei types are similar to that of observed in ZHY with significant changes in the peak values, which is due to the downfield shift. The obtained results clearly indicate the strong interaction between the terminal oxygen of PW_{10} and silanol groups of ZHY.

The unaffected structure of zeolite and uniform dispersion of active species was further confirmed by powder XRD and HRTEM analysis. The XRD pattern of PW_{10}/ZHY was similar to that of support, with retaining the main peaks at 6.35°, 15.8°, 20.6°, 23.7°, 27.1°, 30.8° and 34.2° of FAU type ZHY,[59] along with absences of key characteristic peaks of PW_{10}, confirming homogenous dispersion into the ZHY. Likewise, the uniform dispersion was also observed in HRTEM images of PW_{10}/ZHY, which shows successful anchoring of active species without a significant change in the ZHY structure (Fig. 10). This homogeneous distribution ensures better exposure of active sites while preserving the zeolite structure.

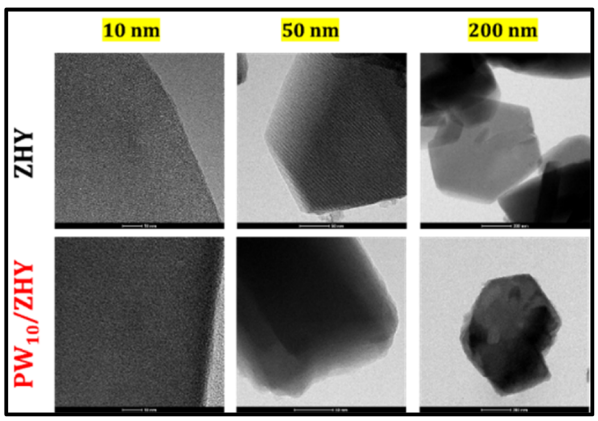

Fig. 10 HRTEM images.

After the detailed cauterization, it is to be noted that the systematic reduction in surface area and pore volume after the synthesis, could potentially point to either pore-mouth blocking or external deposition. However, when seamlessly cross-examined with the XRD, FTIR and HRTEM profiles, simple outer-surface deposition can be completely ruled out. The absolute absence of any characteristic crystalline reflections belonging to bulk PW_{10} in the XRD patterns confirms that the polyoxometalate units are highly isolated and molecularly dispersed without any long-range crystalline agglomeration on the exterior surfaces. Furthermore, HRTEM micrographs reveal immaculate crystal boundaries entirely free of external bulk phase clusters, while FTIR data demonstrate systematic shifts in the internal framework vibrations and hydroxyl regions of the host matrix. When coupled together, these collective findings unequivocally establish that the dilacunary clusters are successfully anchored inside the supercages of the ZHY matrix, stabilized by strong electrostatic interactions with the internal extra-framework host sites rather than undergoing non-specific surface adsorption. In summary, this complete sequence of physical, chemical, acidic, thermal and atomic characterizations conclusively confirms that the dilacunary phosphotungstate clusters have been successfully and uniformly anchored into the accessible microporous cage pathways of zeolite HY without disrupting original structure. This targeted engineering yields a robust heterogeneous interface featuring stable Brønsted acid sites and protected redox active centers. With the structural and textural properties of the catalyst fully mapped and understood, the study next transitions to evaluating its practical performance and selectivity profiles in the solvent-free catalytic oxidation of biomass-derived levulinic acid to succinic acid.

Catalytic evaluation

The oxidation of levulinic acid with hydrogen peroxide was carried out to obtain succinic acid (Scheme 2). These batch performance tests were evaluated to systematically assess the

practical conversion capabilities of our composite interface under target green conditions. Here, the acidity of the catalyst played a role and led to the migration of the less substituted carbon, which resulted in the formation of the tetrahedral intermediate, with subsequent carbon–carbon cleavage to produce succinic acid.

The main reaction parameters were optimized, and their contribution to facilitating the reaction towards selective production of succinic acid is discussed in detail below. Importantly, across all experiments, the selectivity towards succinic acid remained 100%, as here we are getting only a single product. Also, it indicates that changes in reaction parameters influenced only the extent of conversion and not the product pathway.

The effect of different catalyst amounts was studied, and the results are presented in Fig. 11a.

A consistent rise in levulinic acid conversion was observed when the catalyst amount was increased from 25 mg (16%) to 50 mg (19%), and further to 75 mg, achieving a maximum of 26% conversion. This enhancement can be attributed to the greater availability of active acid sites, which facilitates more effective contact between reactant molecules and the catalyst surface. However, a further increase to 100 mg did not lead to any noticeable improvement in conversion (25%). This could be due to saturation of the active sites, where the reactant availability becomes the limiting factor rather than the catalyst amount. Importantly, across all tested loadings, the selectivity towards the succinic acid remained consistently high (100%), indicating that changes in catalyst amount influenced only the extent of conversion and not the product pathway. This plateau addresses the fundamental principle that while the reaction rate in heterogeneous catalysis is ideally proportional to the number of active sites, physical constraints often lead to deviations at higher loadings. In this solvent-free system, the levelling off suggests that once a sufficient number of sites are provided, the overall rate becomes limited by the diffusion of the bulky levulinic acid molecules to the active centers within the zeolite pores rather than the total catalyst quantity. Importantly, across all tested amounts, the selectivity towards succinic acid remained consistently high, indicating that changes in catalyst amount influenced only the extent of conversion and not the reaction pathway. Based on these observations, 75 mg of catalyst was selected as the optimum amount for further studies.

Preliminary investigations using molecular oxygen (O_2) as the oxidant were also conducted; however, the conversion was found to be 4–5% lower than that achieved with hydrogen peroxide. This comparative gas-vs-liquid oxidant test was run to pinpoint the most effective oxygen-transfer medium for activating the target molecule. Given the higher efficiency, ease of handling in the liquid phase, and the benign nature of the water byproduct, H_2O_2 was selected as the optimal oxidant to ensure high accuracy and reproducibility of the reaction kinetics.

To investigate the influence of oxidant concentration and to establish both the optimal conditions and the underlying kinetic behaviour, the molar ratio of levulinic acid to hydrogen peroxide was varied from 1 : 1 to 1 : 4 (Fig. 11b).

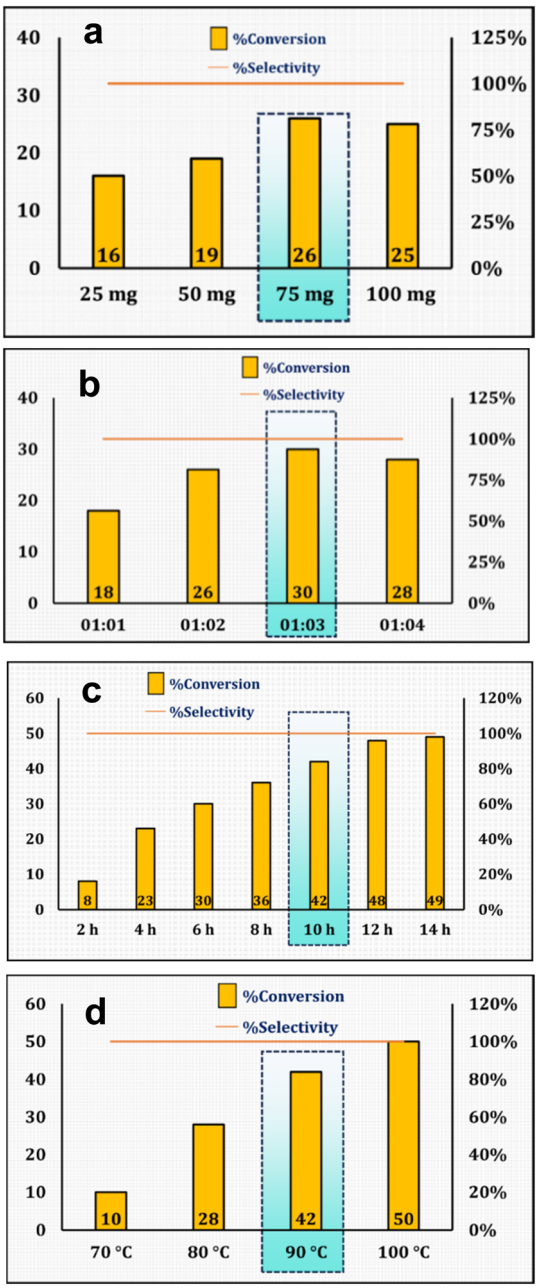

Fig. 11 (a) Reaction conditions. Mole ratio 1 : 2, time 6 h, temp. 90 °C. (b) Reaction conditions. Catalyst amount 75 mg, time 6 h, temp. 90 °C. (c) Reaction conditions. Catalyst amount 75 mg, mole ratio 1 : 3, temp. 90 °C. (d) Reaction conditions. Catalyst amount 75 mg, mole ratio 1 : 3, time 10 h.

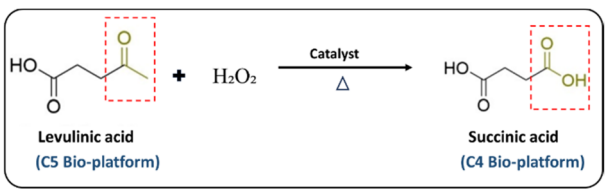

Scheme 2 Oxidation of levulinic acid to produce succinic acid.

An increasing trend in conversion was observed with rising H_2O_2 amount up to a 1 : 3 ratio, where the maximum conversion of 30% was achieved. Kinetically, this enhancement is attributed to the increased generation of electrophilic peroxo-tungstate species on the catalyst surface, which accelerates the oxidative attack on the levulinic acid carbonyl group. The initial positive correlation between H_2O_2 concentration and conversion suggests that the formation of these active oxygen species is a significant factor in the overall reaction rate. However, a slight decline in conversion was noted at a 1 : 4 ratio, likely stems from a kinetic regime where the excessive presence of water and oxidant molecules leads to competitive adsorption on the active sites. This competition, coupled with the dilution of the substrate in the solvent-free system, restricts the accessibility of levulinic acid to the tungsten centers, thereby inhibiting the rate at higher oxidant concentrations. Based on these results, the 1 : 3 mole ratio was identified as the optimum condition, balancing maximum conversion and complete selectivity.

The impact of reaction time was studied over a time range of 2 to 14 hours (Fig. 11c).

A steady increase in conversion was observed with prolonged reaction time, indicating the time-dependent nature of the catalytic transformation. The conversion was increased significantly from 8% to 42% within 10 hours. This steady increase suggests that the oxidation pathway, involving intermediate formation and cleavage, requires sufficient time. At 12 and 14 hours, the conversion increased marginally to 48% and 49%, respectively. This limited improvement beyond 10 hours indicates that the system may have reached an equilibrium. Hence, 10 hours was found to be optimum.

A set of temperature-dependent experiments was conducted to investigate the effect of reaction temperature on levulinic acid conversion. As shown in the Fig. 11d and a progressive increase in temperature led to a notable enhancement in conversion, with the maximum conversion of 50% observed at 100 °C. Although an increased conversion was achieved at 100 °C, 90 °C was identified as the optimal temperature to minimize the thermal decomposition of H_2O_2 and ensure better energy efficiency while maintaining 100% selectivity toward succinic acid, balancing both activity and energy efficiency for the process.

To further understand the nature of the levulinic acid oxidation, the thermodynamic feasibility of the process was considered. Typically, liquid-phase oxidations using H_2O_2 are characterized by a strongly negative Gibbs free energy ($\Delta G < 0$), with the standard Gibbs free energy change for this oxidative cleavage system calculated to be -585.9 kJ mol^{-1} based on standard energies of formation. This large negative value making the transformation of the C5 substrate to C4 succinic acid and C1 byproducts an exergonic and essentially irreversible process. Therefore, the reaction is quantitatively proven not to be restricted by thermodynamic equilibrium, ruling out an equilibrium bottleneck as a reason for the moderate experimental conversions. The observed conversions are instead governed by kinetic factors, such as the activation energy barrier of the Baeyer–Villiger rearrangement and the effective concentration of the peroxo-tungstate intermediates on the catalyst surface.

Based on the above experiments, the maximum 42% conversion and 42% yield was found to be optimum along with the 100% selectivity of succinic acid by employing these optimized parameters: 1 : 3/75 mg/10 hours/90 °C The turnover number was calculated and found to be 462.

The GC and GC-MS profiles are given in SI Fig. 3 and 4 respectively. A satisfactory liquid-phase carbon balance (>90%) was obtained based on GC analysis. No additional peaks corresponding to possible oxidation intermediates were detected in GC-MS analysis. Considering the C5 structure of levulinic acid and the formation of C4 succinic acid, the transformation necessarily involves oxidative C–C bond cleavage. The methyl carbon adjacent to the ketonic carbonyl group (–CO–CH_3 moiety) is proposed to undergo oxidative activation, leading to C–C bond scission and formation of succinic acid. Consistent with the possible oxidation routes summarized in Fig. 2, this cleavage results in the liberation of a C1 byproduct. While no other liquid-phase by-products or intermediate C1 species (such as formic acid) were detected by GC, the overall mass balance is accounted for by the stoichiometric evolution of CO_2 gas. This suggests complete selectivity toward succinic acid within the liquid phase, while the 'missing' carbon fragment is fully oxidized and eliminated from the system as CO_2, which is a typical feature of the oxidative decarboxylation pathway.

To evaluate the kinetic behaviour of the system, the apparent activation energy was determined across the temperature range of 70 to 100 °C with different time intervals using the Arrhenius plot. The reaction followed a pseudo first-order kinetics with respect to levulinic acid concentration, under conditions of excess oxidant. For the oxidative cleavage of levulinic acid, the activation energy was calculated to be 54 kJ mol^{-1} (SI Fig. 5). This value indicates a mixed kinetic regime, meaning the overall reaction rate is co-governed by both the intrinsic chemical reaction at the peroxo-tungstate active sites and the intraparticle mass-transport diffusion of the reactants within the zeolite pores. This kinetic boundary explains the necessity of the 10 h reaction time to achieve the desired conversion while safely preserving the absolute product selectivity.

While establishing these ideal reaction conditions optimizes the visible conversion of levulinic acid, it only reveals half of the catalytic profile. To verify the true economic efficiency of the present system and determine exactly how much peroxide is constructively utilized by the active tungsten centers *versus* how much is wasted through thermal degradation, an independent quantification of the remaining oxidant was required. Consequently, immediately following the completion of the optimized reaction run, an iodometric titration was carried out on the residual mixture to measure the residual H_2O_2 after completion of the reaction. This quantitative measurement was executed because tracking the exact amount of remaining peroxide allows us to calculate the active oxidant utilization efficiency and distinguish between productive oxygen transfer to the substrate *versus* unproductive thermal decomposition. In which, the reaction mixture was filtered and treated with potassium iodide in acidic medium. The liberated iodine was

further titrated against standardized $Na_2S_2O_3$ using starch as an indicator. It was found that about 4.0 mmol of H_2O_2 remained in the system after 10 hours compared to that of the 4.2 mmol required for the optimized conversion. The data indicates that the majority of the H_2O_2 was used for activating the redox centers of PW_{10}. This indicates that while some decomposition occurs, primarily due to the thermal sensitivity of the oxidant and the presence of redox-active metal sites, a significant portion is effectively channelled into the formation of active peroxo-tungstate species. The choice of 90 °C serves as a kinetic compromise, higher temperatures slightly increased conversion but also accelerated the unproductive disproportionation of H_2O_2 into O_2 and H_2O, thereby reducing the overall oxidant efficiency. This quantitative assessment of residual H_2O_2 suggests a high degree of oxidant efficiency, with minimal unproductive decomposition into. The fact that 4.0 mmol remained out of the excess provided, while nearly the stoichiometric amount (4.2 mmol) was consumed for the conversion, confirms that the catalyst facilitates a controlled activation of the peroxide. Specifically, the redox-active tungsten sites favor the formation of electrophilic peroxo-species, the key intermediates for C–C bond cleavage in levulinic acid over the radical-mediated decomposition pathways typically seen in less selective systems. Furthermore, the absence of vigorous gas evolution during the reaction supports the conclusion that the catalytic cycle is dominated by the productive oxygen-transfer process rather than thermal or catalytic disproportionation of the oxidant.

Even though the levulinic acid conversion remains moderate, the strength of this system lies in its remarkable cleanliness and practicality. The reaction channels the substrate entirely toward succinic acid, delivering absolute selectivity without any detectable secondary products. This outcome is made possible through the use of hydrogen peroxide, an environmentally friendly oxidant that aligns well with green chemistry principles. Importantly, the whole process functions efficiently in a simple batch reactor, avoiding the need for costly equipment, hazardous chemicals or volatile solvents. Operating under mild conditions, the method keeps energy consumption low while ensuring safer handling. Altogether, the approach demonstrates how a straightforward, sustainable setup can still achieve a highly precise transformation.

However, it is crucial to discuss that while the levulinic acid conversion remains moderate over a prolonged reaction time, this performance reflects a fundamental engineering trade-off inherent to highly selective, solvent-free heterogeneous systems. Traditional homogeneous polyoxometalate or mineral acid catalysts frequently report higher conversion rates in shorter times; however, they rely heavily on volatile organic solvents, suffer from severe active-phase leaching, require energy-intensive downstream distillation, and generate significant chemical waste (high E-factors). In contrast, the present catalyst eliminates organic solvents entirely. The moderate conversion and extended reaction window are primarily governed by intraparticle mass-transfer limitations, as levulinic acid molecules must slowly diffuse through the restricted microporous channels of the zeolite host to reach the active cages. Nevertheless, this diffusion constraint acts as a kinetic regulator that prevents over-oxidation, ensuring an exceptional selectivity to succinic acid and allowing for effortless catalyst separation and recycling.

Table 2 Control experiments[a]

	Levulinic acid oxidation	
Materials	% Conversion	% Selectivity
[1]ZHY	—	—
[2]PW_{10}	31	100
[3]PW_{10}/ZHY	42	100

[a] Reaction conditions: 1 : 3 mole ratio/[1] 17.4, [2] 57.6, [3] 75 mg/90 °C/10 h.

Control experiments

The role of PW_{10} and ZHY was studied both individually and synergistically, and the results are given in Table 2. The reaction performed with only ZHY resulted in no observable conversion of levulinic acid, confirming that the zeolite support itself does not possess sufficient oxidative activity.

In contrast, alone PW_{10} exhibited 31% conversion with 100% selectivity, indicating its inherent oxidative capability. Notably, PW_{10}/ZHY showed enhanced performance with 42% conversion and complete selectivity. The superior activity of the catalyst is likely associated with its di-lacunary structure, which provides additional coordination sites and higher surface oxygen vacancies. These structural features facilitate the interaction with H_2O_2, promote the generation of active peroxo or oxo species, and enable better substrate activation during oxidation. Furthermore, the synergy between the di-lacunary phosphotungstates and the microporous zeolite matrix thus leads to improved catalytic performance significantly proved the heterogeneous nature of the catalyst.

While establishing this synergistic relationship points toward a highly active heterogeneous boundary, the precise underlying chemical mechanism must be unravelled. Having confirmed that the combination of the support and PW_{10} drives this active phase transformation, the identity of the transient oxygen species operating at this interface must be uncovered. To trace whether the reaction proceeds *via* an open-shell radical pathway or a coordinated surface transfer, radical scavenger experiments were explored.

Scavenger experiments

To further probe the nature of the active oxidizing species, radical scavenger experiments[60,61] were conducted under optimized reaction conditions (Table 3). Isopropanol (IPA) or *tert*-butanol (*t*-BuOH) was added to the reaction mixture as radical scavenger in amounts of 10 mmol prior to heating. These chemical intervention tests were systematically carried out to selectively quench specific radical intermediates, directly establishing whether the reaction route. Reactions were run for the same time as standard experiments and conversion/selectivity were determined by GC. All scavenger runs were

Table 3 Scavenger experiments in oxidation

Entry	Condition/scavenger	Observation	Conversion (%)
1	Without scavenger	—	42
2	+ IPA (10 mmol)	Strong inhibition with moderate $^{\bullet}OH$ scavenging	12
3	+ *t*-BuOH (10 mmol)	Partial inhibition with moderate $^{\bullet}OH$ scavenging	21

performed twice. The addition of IPA/*t*-BuOH ($^{\bullet}OH$ scavenger) resulted in a marked decrease in the conversion of levulinic acid, indicating that surface-confined radical networks act as the primary driving species governing the transformation. To clearly reconcile this behaviour, the catalytic mechanism is proposed to operate *via* a surface-confined homolytic sequence. Initially, the interaction between H_2O_2 and the di-lacunary tungsten centers proceeds *via* a a localized activation pathway, where hydrogen peroxide coordinates to the vacant tungsten sites to form an electrophilic peroxo-tungstate species. However, due to the high density of surrounding framework Brønsted acid sites and thermal energy, this surface-bound peroxo complex undergoes a localized, homolytic O–O bond cleavage or a surface-assisted single-electron transfer. This process generates cage-confined hydroxyl radical pairs trapped near the tungsten coordination sphere. Because these radicals are heavily restricted inside the zeolite supercages (the confinement effect), they do not escape into the bulk solution to cause random, non-selective decomposition. Instead, they remain highly directed, specifically abstracting hydrogen from the levulinic acid substrate molecule to initiate the selective C–C bond cleavage. This accounts for why the addition of radical scavengers like IPA shows such powerful inhibition, while the system still maintains an absolute 100% selectivity toward succinic acid without byproduct formation.

This study indicate that hydroxyl radicals are the principal oxidizing species. Addition of scavenger reduced levulinic acid conversion. It was observed that the inhibition was more pronounced with IPA than with *t*-BuOH. This is consistent with kinetic trends for $^{\bullet}OH$ reactions: IPA (secondary alcohol) reacts more rapidly with $^{\bullet}OH$ than the sterically hindered *t*-BuOH, so IPA removes the radical pool more effectively, giving a larger decrease in conversion.

Furthermore, the possibility of the scavengers acting as surface-blocking agents rather than chemical quenchers can be ruled out based on steric considerations. Although *t*-BuOH is more sterically hindered and bulkier than IPA, it exhibited a lower inhibitory effect (21% conversion *vs.* 12% for IPA). If physical adsorption on the catalyst surface were the primary cause of inhibition, the bulkier *t*-BuOH would logically lead to a greater reduction in activity. Thus, the observed trend confirms that the inhibition is indeed a result of radical scavenging.

Defining this radical-assisted oxidation mechanism completes the fundamental chemical characterization of the reaction line. To bridge the gap between these benchtop mechanistic findings and actual practical utility, the system must be examined under a chemical engineering lens. A genuinely sustainable process must demonstrate manufacturing feasibility; hence, the reaction parameters were scaled up to quantitatively measure its alignment with industrial efficiency indices.

Industrial relevance & Green Engineering: a step towards sustainability

In order to find out the compatibility towards industrial sectors of the present catalytic system, the scale-up experiments were carried out and the obtained results are summarized in the Table 4. It was found that the observed results after scale-up are consistent with the batch scale experiments which reveals the high adaptability of catalyst towards large scale productions without comprising its activity. The green metrics calculated for the system demonstrate satisfactory material efficiency at the reaction level[62,63].

The E-factor was determined to be 3.62, indicating relatively low waste generation and remaining below the commonly accepted value of 5 for fine chemical processes. The reaction process mass intensity (rPMI) of 4.62 falls within the desirable range of 1–5 g g^{-1}, reflecting efficient utilization of reactants. Furthermore, the atom economy of 79% suggests that a substantial portion of the reactant mass is incorporated into the desired product, with the value inherently limited by the stoichiometric carbon loss during oxidation. Overall, these metrics collectively indicate a reasonably efficient and material-conscious transformation. The present system demonstrates inherent safety and waste prevention by achieving 100% selectivity under mild conditions, eliminating hazardous by-products. The use of a renewable feedstock combined with a bifunctional composite design simplifies the process by minimizing material diversity and facilitating easy separation. Furthermore, the high mass efficiency and proven catalyst durability underscore a highly sustainable and industrially viable engineering approach, collectively demonstrates high alignment with key important Green Engineering principles (Fig. 12).

Additionally, in support with this, it advances several Green Chemistry principles, including waste prevention (Principle 1)

Table 4 Scale-up experiments

	Reaction conditions			Results	
	LeA (ml)	H_2O_2 (ml)	Cat. Amt (mg)	%Conv.	%Sele.
Optimized	1.09	3.06	75	42	100
Scale up (×2)	2.18	6.12	150	42	100
Scale up (×3)	3.27	9.18	225	43	100
Scale up (×4)	4.36	12.24	300	43	100
Scale up (×5)	5.45	15.30	375	45	100

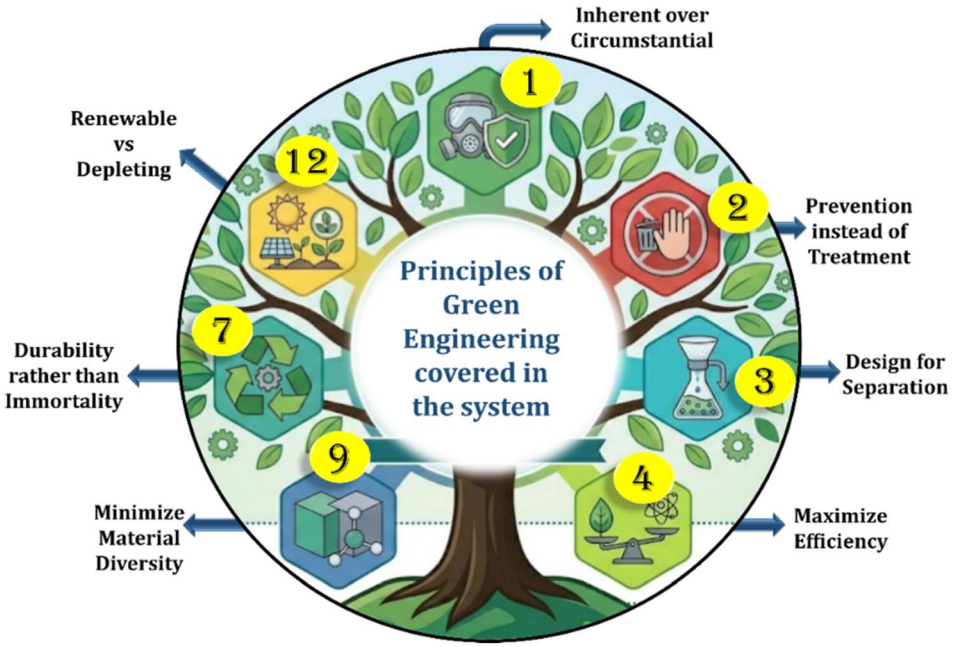

Fig. 12 Contribution and correlation towards Green Engineering Principles.

through complete product selectivity, improved atom economy (Principle 2), reduced hazard *via* the use of hydrogen peroxide as a comparatively benign oxidant (Principle 3), safer solvent selection (Principle 5), energy-efficient operation under mild conditions (Principle 6), utilization of renewable biomass-derived feedstocks (Principle 7), avoidance of unnecessary derivatization (Principle 8), catalytic efficiency (Principle 9) and inherently safer processing conditions (Principle 12). This environmental indexing is highlighted to provide a robust operational baseline for evaluating the potential scalability and technological viability of our catalytic system in modern bio-refineries.

While achieving favourable mass-efficiency indices and green metrics highlights the initial environmental cleanliness of the process, the long-term industrial viability relies fundamentally on the catalyst's lifecycle. A solid contact that degrades rapidly or undergoes irreversible structural collapse cannot sustain a truly green process over time. Therefore, to evaluate the structural endurance and economic feasibility of the composite over multiple cycles, regeneration and reusability profiles were thoroughly investigated.

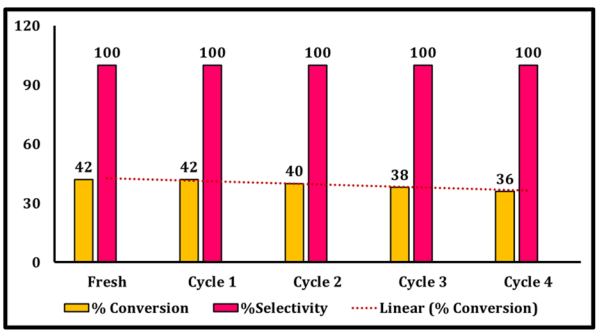

Fig. 13 Recycling experiments.

Regeneration and recycling experiments

After the completion of reaction, the mixture was cooled to room temperature and diluted with methanol and allowed for the centrifugation. The catalyst was then separated, filtered and washed with distilled water followed by an ethanol wash. Further it was dried at 100 °C for 3 hours, and designated as R-PW_{10}/ZHY, and employed for the catalytic run in the optimized conditions. The obtained results are summarized in the Fig. 13.

It was observed that there is 0 to 6% drop found in conversion, however, the selectivity was intact up to 4 consecutive cycles. Further, the stability of the regenerated catalyst was confirmed *via* the acidity measurements (Fig. 14), BET analysis and FTIR (Fig. 15).

The acidity measurement by potentiometric titration revealed that after the regeneration, the acidic strength as well as total acidic sites remained unaffected, proving the sustained and stable nature of the regenerated catalyst. The obtained BET surface area (202 $m^2\ g^{-1}$) was in good agreement with the fresh catalyst. Likewise, the FTIR showed the presence of main characteristic peaks without any significant change in the intensity as well as band ranges, depicting the intact structure.

Comparison

The comparison of present catalyst with reported heterogeneous catalysts for the oxidation of levulinic acid with hydrogen peroxide is given in Table 5. The reported catalysts are unable to achieve higher selectivity of succinic acid. Entry 1 showed 48% conversion by employing mild reaction conditions; however, the catalyst employed was homogeneous. Although they have

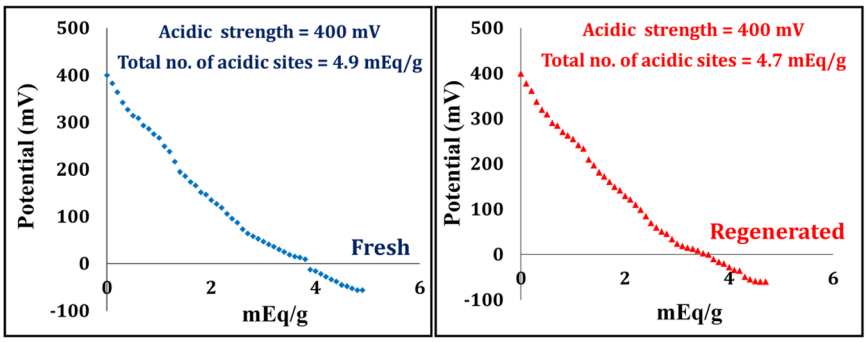

Fig. 14 Potentiometric titration curves of fresh and regenerated catalysts.

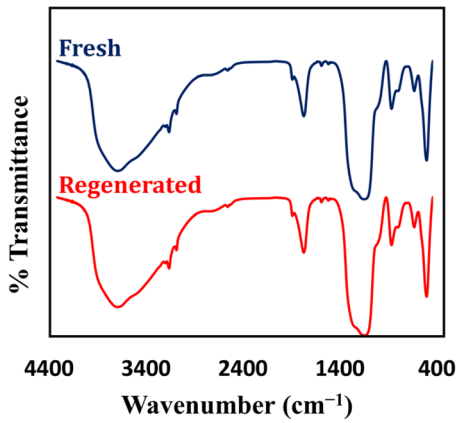

Fig. 15 FTIR spectra of fresh and regenerated catalysts.

reported the recycling but, when the process is subjected to commercialization, it will not be worth recovering homogeneous catalysts as it will be obviously a tricky and multiple steps taking procedure, even though getting a moderate amount of recovery of catalysts, suggesting a high-cost economic process. Whereas, entry 2 showed a set of heterogeneous catalysts but possessing very low conversion/yield even after employing such harsh conditions. PW_{10}/ZHY enables 100% selective oxidation of levulinic acid to succinic acid, with no by-products and excellent recyclability under mild, solvent-free conditions. Unlike other catalysts, it avoids overoxidation and unwanted esters, making this process efficient and environmentally benign.

Interestingly, the comparison with the homogeneous H_2WO_4 system highlights a fundamental advantage of present catalyst that transcends simple conversion metrics. While it reaches 48% conversion, its 75% selectivity implies that 25% of the substrate is converted into unwanted byproducts, necessitating complex, energy-intensive downstream separation and purification. In contrast, PW_{10}/ZHY achieves 100% selectivity, yielding a 'pure-at-source' product stream that significantly reduces the overall process cost and environmental footprint. Furthermore, the trade-off in reaction time and loading is a deliberate and necessary investment for heterogeneity. Unlike the homogeneous system, which is lost as acidic waste after a single use, the present catalyst is easily recovered and maintains stable activity over multiple cycles. In modern sustainable catalysis, the shift from a 'disposable' 75%-selective homogeneous system to a recyclable, 100%-selective heterogeneous interface is a substantial advancement, as the gains in atom economy and reusability far outweigh the marginal differences in initial kinetics.

It is to be noted that, effect of support is playing important role. The supports incorporated in entry 2 are showing lesser activity than entry 3 and 4. However, it is to be noted that in the oxidation reaction ZHY is more effective than ZHβ. The superior catalytic performance is clearly reflected in the experimental results, where the PW_{10} with ZHY achieved a higher conversion of 42% compared to the 37% conversion exhibited by ZHβ based. This enhancement can be attributed to the distinct structural and textural properties of the underlying zeolite frameworks. ZHY possesses a three-dimensional faujasite (FAU) structure characterized by large supercages with an internal diameter of approximately 1.3 nm, accessible *via* 12-membered ring windows of 0.74 nm. This spacious cage configuration

Table 5 Comparison with reported catalytic systems

Entry	Catalyst	LA : H_2O_2/Catalyst amount/time/temp	%Conv.	%Sele.[a]/%Yield of succinic acid[b]	Reference
1	H_2WO_4	1 mmol/5 mmol//25 mg/6 h/90 °C	48%	75%[a]	21
2	Ru/CeO_2	50 mmol/150 mmol/50 mg/—/90 °C	<1%	<1%[b]	26
	Ru/Zeo		1%	<1%[b]	
	Ru/C		20%	2%[b]	
3	PW_{10}/ZHβ	10 mmol/30 mmol/75 mg/10 h/90 °C	37%	100%[a]	52
4	PW_{10}/ZHY	10 mmol/30 mmol/75 mg/10 h/90 °C	42%	100%[a]	Present work

[b] a= % Selectivity of succinic acid. [a] b= % Yield of succinic acid.

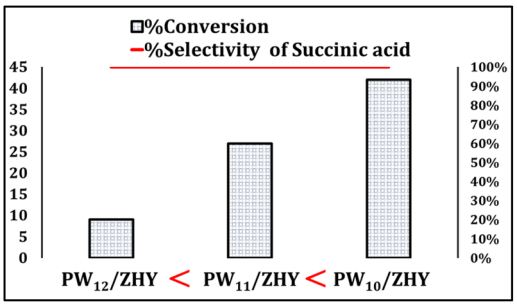

Fig. 16 Order of activity of lacunary and non-lacunary systems.

provides a highly accommodating confined environment that effectively stabilizes the bulky PW_{10} clusters while maintaining excellent molecular diffusion pathways for the levulinic acid reactant. In contrast, ZHβ features an interconnected channel system (BEA topology) lacking these distinct supercages, which restricts the optimal dispersion and isolation of the active polyoxometalate phases. Furthermore, the characteristic acid site density within the ZHY framework exerts a stronger cooperative electronic effect with the PW_{10} species, accelerating the multi-electron redox transfers necessary to push the conversion from 37% up to 42%.

Also, it is interesting to note down that, the reaction was performed with non-lacunary and mono lacunary system also to understand the activity of POMs series in oxidation. The obtained results are presented in Fig. 16. It was found that the observed trend in catalytic activity follows the order: PW_{12} < PW_{11} < PW_{10}, which reflects the progressive increase in catalytic performance with increasing lacunarity in the Keggin structure. This superior performance can be attributed to the di-lacunary nature of PW_{10} which introduces unsaturated coordination sites that act as efficient active centers for oxidation. Whereas parent PW_{12} reflects poor conversion due to their fully saturated parent Keggin structure, which limits activation of the oxidant and hinders substrate accessibility. Similarly, PW_{11}/ZHY demonstrated moderate conversion, but was comparatively higher than the parent system due to the lacuna present in the structure.

Plausible reaction mechanism

For the oxidation reaction, a synergistic interaction between redox-active centers and surface acidity of the present catalyst facilitated the succinic acid formation by the well-known Baeyer–Villiger oxidation pathway. Literature reports have proposed the formation of succinic acid through intermediate methyl succinate, often attributed to esterification and subsequent hydrolysis in the presence of methanol or related solvent systems.[21,26] However, in the present study, we expect an alternative mechanistic pathway as follows: Fig. 17 shows the steps involved in the selective production of succinic acid.

Initially, adsorption of levulinic acid takes place on the surface of the catalyst *via* hydrogen bonding between carbonyl oxygen of acid and silanol groups of catalyst. The unique structure and confined pore environment of zeolite directs the reactants near to the redox-active W centers which facilitates the

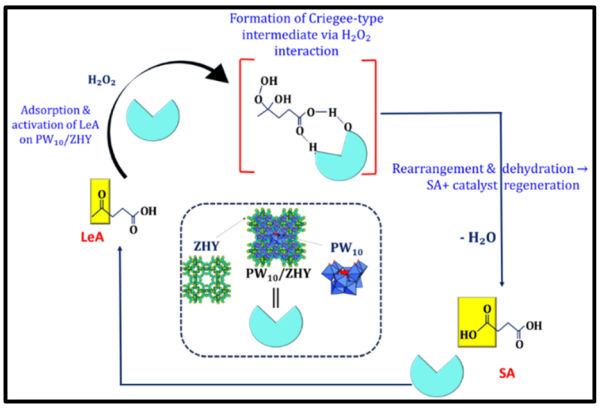

Fig. 17 Plausible reaction mechanism for oxidation of levulinic acid.

interaction and stabilizes the transition states. Interestingly, when the catalyst reacted with hydrogen peroxide, the interaction of H_2O_2 with the PW_{10} centers initiates a homolytic activation pathway, generating highly active, surface-bound peroxotungsten radical species [W–OO], which can transfer an activated oxygen atom. After that, the activated oxygen of this coordinated radical species attacks the carbonyl carbon of levulinic acid which resulted into the formation of a localized, radical-type Criegee-like tetrahedral intermediate, that further stabilized by coordination to the tungsten center and hydrogen bonding with the zeolite hydroxyl groups. Subsequently, Brønsted acid sites from catalyst protonate the peroxy oxygen, enabling cleavage of the O–O bond, initiating a radical-mediated Baeyer–Villiger-type homolytic rearrangement, wherein the $–CH_2–CH_2–COOH$ group migrates to the electron-deficient oxygen, introducing an additional oxygen atom into the molecular framework. This rearrangement, followed by hydrolysis and proton transfer, results in the formation of succinic acid ($HOOC–CH_2–CH_2–COOH$). The homolytic nature of this rearrangement is strongly supported by the quenching studies, confirming that these surface-confined radical species drive the transformation.

Crucially, because these radical intermediates are confined within the faujasite cages rather than freely diffusing in the bulk phase, they are completely prevented from undergoing unselective degradation. This structural confinement perfectly channels the radical network into a highly directed pathway. During this oxidative C–C bond cleavage, the methyl group of the levulinic acid is liberated as a C1 byproduct. While GC-MS analysis of the liquid phase showed no detectable side-products like formic acid, the reaction stoichiometry and the observed carbon balance indicate that this C1 fragment undergoes deep oxidation to CO_2 gas. This is consistent with the Baeyer–Villiger-type pathway under the current oxidative conditions, where the evolution of CO_2 is the final step in the mineralization of the single-carbon fragment.

Overall, the reaction governs the synergistic cooperation of the redox-active PW_{10} and the acidic–structural environment of ZHY, enabling the selective and efficient solvent-free oxidation of levulinic acid to succinic acid.

Conclusions

In conclusion, the results emphasize the importance of engineered inorganic interfaces in governing reactivity and selectivity in oxidation processes. Using hydrogen peroxide as a green oxidant, the PW_{10}/ZHY catalyst enabled complete product selectivity of succinic acid while avoiding overoxidation or undesired by-products. Although the %yield of levulinic acid was 42%, which is moderate, control and scavenger experiments confirmed that hydroxyl radicals act as the primary oxidizing species, with stronger inhibition by isopropanol supporting their higher reactivity toward $^{\bullet}OH$. Ultimately, the major value-added of this study is the benchmark achievement of 100% product selectivity, establishing a transformative design where the structural confinement of inorganic catalyst is strategically exploited to completely suppress thermodynamic over-oxidation pathways. The combined redox character of the PW_{10} units and the acidic, confined environment of zeolite HY played a critical role in substrate activation, intermediate stabilization, and pathway direction. The catalyst retained its structural integrity and activity over multiple cycles, underscoring its robustness. Comparative analysis highlights the advantages of this approach over previous reports, particularly in terms of operational simplicity, sustainable reaction conditions, and precise control over product formation. A mechanistic interpretation consistent with a Baeyer–Villiger-type pathway is proposed to rationalize the observed selectivity. The scientific significance of validating this specific radical-mediated pathway lies in shifting the paradigm of complex biomass oxidation, it proves that notoriously unselective radical networks can be precisely governed to cleave specific carbon–carbon bonds. This fundamental insight into PW_{10}-ZHY synergy bridges the gap between heterogeneous material design and precise molecular regulation. Overall, this study presents a practical and mechanistically unique pathway for the C5-to-C4 conversion of a key bioplatform molecule, emphasizing the scientific merit and novelty of the approach. Additionally, such combinations of materials can be beneficial for future design of inorganic hybrid systems with tailored structure–property relationships for selective transformations.

Author contributions

Anjali Patel: conceptualization, validation, writing – review & editing, visualization, supervision. Margi Joshi: methodology, data curation, validation, formal analysis, investigation, writing – original draft.

Conflicts of interest

There are no conflicts to declare.

Abbreviations

POMs	Polyoxometalates
PW_{10}	Dilacunary phosphotungstate
PW_{11}	Mono lacunary phosphotungstate
PW_{12}	parent phosphotungstic acid
ZHY	Zeolite HY
FAU	Faujasite framework geometry
FTIR	Fourier transform infrared spectroscopy
TGA	Thermogravimetric analysis
BET	Brunauer–Emmett–Teller
XRD	X-ray diffraction
HRTEM	High-resolution transmission electron microscopy
TPD	Temperature programmed desorption
EDS	Energy-dispersive X-ray spectroscopy
MAS-NMR	Magic angle spinning nuclear magnetic resonance
ICP	Inductively coupled plasma
LeA	Levulinic acid
SA	Succinic acid
IPA	Isopropyl alcohol (isopropanol)
t-BuOH	*Tert*-butyl alcohol
ΔG	Gibbs free energy
E-factors	Environmental factor
GC	Gas chromatography
GC-MS	Gas chromatography–mass spectrometry
TON	Turnover number
rPMI	Reaction process mass intensity

Data availability

The data supporting this article have been included as part of the supplementary information (SI). Supplementary information: it contains detailed procedures for catalyst synthesis and catalytic activity. Additionally, FT-IR of support, XRD, GC and GC-MS profiles, kinetics plot are given in SI Fig. 1, 2, 3, 4 and 5 respectively. See DOI: https://doi.org/10.1039/d6ra03282f.

Acknowledgements

AP and MJ are thankful to the Department of Chemistry, The Maharaja Sayajirao University of Baroda for the infrastructural facilities and DST-FIST for BET surface area analysis.

References

1 S. E. Davis, M. S. Ide and R. J. Davis, *Green Chem.*, 2013, **15**, 17–45, DOI: 10.1039/C2GC36441G.
2 K. Hatakeyama, Y. Nakagawa, M. Tamura and K. Tomishige, *Green Chem.*, 2020, **22**, 4962–4974, DOI: 10.1039/D0GC01277G.
3 K. T. Venkateswara Rao, B. Haribabu, P. S. Sai Prasad and N. Lingaiah, *Green Chem.*, 2013, **15**, 837, DOI: 10.1039/c3gc36735e.
4 J. Teržan, A. Sedminek, Ž. Lavrič, M. Grilc, M. Huš and B. Likozar, *Green Chem.*, 2023, **25**, 2220–2240, DOI: 10.1039/D2GC04623G.
5 B. Stanje, P. Traar, J. A. Schachner, F. Belaj and N. C. Mösch-Zanetti, *Dalton Trans.*, 2018, **47**, 6412–6420, DOI: 10.1039/C8DT00819A.
6 S. Wang, X. Li, C. Lai, Y. Zhang, X. Lin and S. Ding, *RSC Adv.*, 2024, **14**, 30566–30581, DOI: 10.1039/D4RA05102E.

7 A. S. Sharma, H. Kaur and D. Shah, *RSC Adv.*, 2016, **6**, 28688–28727, DOI: 10.1039/C5RA25646A.
8 S. G. Yao, M. S. Meier, R. B. Pace III and M. Crocker, *RSC Adv.*, 2016, **6**, 104742–104753, DOI: 10.1039/C6RA18806K.
9 B. Maleki, H. Kamyab and M. Yusuf, in *Development of Heterogeneous/Nanocatalysts in Biodiesel Production*, Royal Society of Chemistry, 2024, pp. 188–210, DOI: 10.1039/BK9781837672530-00188.
10 T. Gao, Y. Yin, W. Fang and Q. Cao, *Mol. Catal.*, 2018, **450**, 55–64, DOI: 10.1016/j.mcat.2018.03.006.
11 Y. An, T. Lei, W. Jiang and H. Pang, *Green Chem.*, 2024, **26**, 10739–10773, DOI: 10.1039/D4GC03597F.
12 Y. Shen, W. Guo, Z. Tu, Q. Han, Z. Ou, J. Chen, R. Hu and Z. Hu, *J. Environ. Chem. Eng.*, 2026, **14**, 120587, DOI: 10.1016/j.jece.2025.120587.
13 H. Kamyab, T. Khademi, S. Chelliapan, M. Yusuf, S. Rajendran and M. Shekofteh-Gohari, *Mater. Res. Bull.*, 2026, **197**, 113961, DOI: 10.1016/j.materresbull.2025.113961.
14 S. Dutta, L. Wu and M. Mascal, *Green Chem.*, 2015, **17**, 2335–2338, DOI: 10.1039/C5GC00098J.
15 F. D. Pileidis and M. Titirici, *ChemSusChem*, 2016, **9**, 562–582, DOI: 10.1002/cssc.201501405.
16 F. Xia, Z. Du, J. Liu, Y. Ma and J. Xu, *RSC Adv.*, 2016, **6**, 72744–72749, DOI: 10.1039/C6RA16149A.
17 T. R. dos Santos, P. Nilges, W. Sauter, F. Harnisch and U. Schröder, *RSC Adv.*, 2015, **5**, 26634–26643, DOI: 10.1039/C4RA16303F.
18 A. Chatzidimitriou and J. Q. Bond, *Green Chem.*, 2015, **17**, 4367–4376, DOI: 10.1039/C5GC01000D.
19 R. Zhu, A. Chatzidimitriou, B. Liu, D. J. Kerwood and J. Q. Bond, *ACS Catal.*, 2020, **10**, 1555–1565, DOI: 10.1021/acscatal.9b04289.
20 J. Mao, D. Wang, C. Zhang, Y. Xie, Q. Song, B. Zhang, Y. Lou, C. Pan, J. Zhang, Y. Zhang and Y. Zhu, *Chem Catal.*, 2025, **5**, 101415, DOI: 10.1016/j.checat.2025.101415.
21 D. Carnevali, M. G. Rigamonti, T. Tabanelli, G. S. Patience and F. Cavani, *Appl. Catal., A*, 2018, **563**, 98–104, DOI: 10.1016/j.apcata.2018.06.034.
22 H. Choudhary, S. Nishimura and K. Ebitani, *Appl. Catal., A*, 2013, **458**, 55–62, DOI: 10.1016/j.apcata.2013.03.033.
23 J. M. Pinazo, M. E. Domine, V. Parvulescu and F. Petru, *Catal. Today*, 2015, **239**, 17–24, DOI: 10.1016/j.cattod.2014.05.035.
24 C. Delhomme, D. Weuster-Botz and F. E. Kühn, *Green Chem.*, 2009, **11**, 13–26, DOI: 10.1039/B810684C.
25 H. Asim, H. Zeidan and M. E. Marti, *RSC Adv.*, 2024, **14**, 16765–16777, DOI: 10.1039/D4RA02110J.
26 L. A. Arriaga-Arellano, D. Álvarez-Hernández, M. I. Domínguez, M. Martínez T, A. Penkova, S. Ivanova and M. Á. Centeno, *Next Mater.*, 2024, **3**, 100059, DOI: 10.1016/j.nxmate.2023.100059.
27 A. P. Dunlop and S. Smith, Preparation of succinic acid, *US Pat.*, US2676186A, 1954.
28 I. Podolean, V. Kuncser, N. Gheorghe, D. Macovei, V. I. Parvulescu and S. M. Coman, *Green Chem.*, 2013, **15**, 3077, DOI: 10.1039/c3gc41120f.
29 R. Kawasumi, S. Narita, K. Miyamoto, K. Tominaga, R. Takita and M. Uchiyama, *Sci. Rep.*, 2017, **7**, 17967, DOI: 10.1038/s41598-017-17116-4.
30 F. Mohamadpour, H. Kamyab, S. Chelliapan and A. M. Amani, *Org. Prep. Proced. Int.*, 2025, **57**, 239–245, DOI: 10.1080/00304948.2024.2429511.
31 J. Albert, D. Lüders, A. Bösmann, D. M. Guldi and P. Wasserscheid, *Green Chem.*, 2014, **16**, 226–237, DOI: 10.1039/C3GC41320A.
32 T.-Y. Dang, R.-H. Li, H.-R. Tian, Q. Wang, Y. Lu and S.-X. Liu, *Inorg. Chem. Front.*, 2021, **8**, 4367–4375, DOI: 10.1039/D1QI00799H.
33 J.-J. Ye and C.-D. Wu, *Dalton Trans.*, 2016, **45**, 10101–10112, DOI: 10.1039/C6DT01378C.
34 S. Yan, Y. Li, P. Li, T. Jia, S. Wang and X. Wang, *RSC Adv.*, 2018, **8**, 3499–3511, DOI: 10.1039/C7RA12842H.
35 M. Alizadeh and B. Yadollahi, *RSC Adv.*, 2025, **15**, 8777–8783, DOI: 10.1039/D5RA00821B.
36 E. Naseri and R. Khoshnavazi, *RSC Adv.*, 2018, **8**, 28249–28260, DOI: 10.1039/C8RA03659D.
37 C. Li, K. Yamaguchi and K. Suzuki, *Angew. Chem.*, 2021, **133**, 7036–7040, DOI: 10.1002/ange.202016642.
38 J.-C. Raabe, T. Esser, F. Jameel, M. Stein, J. Albert and M. J. Poller, *Inorg. Chem. Front.*, 2023, **10**, 4854–4868, DOI: 10.1039/D3QI00937H.
39 N. C. Coronel and M. J. da Silva, *J. Cluster Sci.*, 2018, **29**, 195–205, DOI: 10.1007/s10876-018-1343-0.
40 A. Modvig, C. Kumpidet, A. Riisager and J. Albert, *Materials*, 2019, **12**, 2175, DOI: 10.3390/ma12132175.
41 Z. Yekke-Ghasemi, M. M. Heravi, M. Malmir, G. Jahani, M. B. Bisafar and M. Mirzaei, *Inorg. Chem. Commun.*, 2022, **140**, 109456, DOI: 10.1016/j.inoche.2022.109456.
42 A. Kumar, W. S. C. Ming, P. Ramsaroop, S. A. Dhanpat, M. Forde, D. Pathak and V. Kumar, *Appl. Catal., A*, 2025, **704**, 120406, DOI: 10.1016/j.apcata.2025.120406.
43 S. P. Teong, X. Li and Y. Zhang, *Green Chem.*, 2019, **21**, 5753–5780, DOI: 10.1039/C9GC02445J.
44 A. Podgoršek, M. Zupan and J. Iskra, *Angew. Chem., Int. Ed.*, 2009, **48**, 8424–8450, DOI: 10.1002/anie.200901223.
45 X. Hao, O. Yamazaki, A. Yoshida and J. Nishikido, *Green Chem.*, 2003, **5**, 524–528, DOI: 10.1039/B304439D.
46 B. Martin, J. Sedelmeier, A. Bouisseau, P. Fernandez-Rodriguez, J. Haber, F. Kleinbeck, S. Kamptmann, F. Susanne, P. Hoehn, M. Lanz, L. Pellegatti, F. Venturoni, J. Robertson, M. C. Willis and B. Schenkel, *Green Chem.*, 2017, **19**, 1439–1448, DOI: 10.1039/C6GC02899C.
47 Y. Yamada, Y. Miwa, Y. Toyoda, Y. Uno, Q. M. Phung and K. Tanaka, *Dalton Trans.*, 2024, **53**, 6556–6567, DOI: 10.1039/D3DT04313D.
48 C. B. Vilanculo, M. J. da Silva, A. A. Rodrigues, S. O. Ferreira and R. C. da Silva, *RSC Adv.*, 2021, **11**, 24072–24085, DOI: 10.1039/D1RA04191F.
49 S. Xue, G. Chen, Z. Long, Y. Zhou and J. Wang, *RSC Adv.*, 2015, **5**, 19306–19314, DOI: 10.1039/C4RA15921G.
50 H. Wang, Y. Poya, X. Chen, T. Jia, X. Wang and J. Shi, *RSC Adv.*, 2015, **5**, 45725–45730, DOI: 10.1039/C5RA07747H.

51 N. Alonso-Fagúndez, I. Agirrezabal-Telleria, P. L. Arias, J. L. G. Fierro, R. Mariscal and M. L. Granados, *RSC Adv.*, 2014, **4**, 54960–54972, DOI: 10.1039/C4RA11563E.
52 A. Patel and M. Joshi, *Catal. Sci. Technol.*, 2026, **16**, 3236–3254, DOI: 10.1039/D5CY01399B.
53 G. D. Yadav and V. V. Bokade, *Appl. Catal., A*, 1996, **147**, 299–323, DOI: 10.1016/S0926860X(96)00206-2.
54 A. Patel and M. Joshi, *New J. Chem.*, 2025, **49**, 1251–1261, DOI: 10.1039/D4NJ04968C.
55 T. Furusawa, K. Kimura, K. Matsutani, K. Akiyama and T. Sugiyama, *Int. J. Hydrogen Energy*, 2023, **48**, 29629–29640, DOI: 10.1016/j.ijhydene.2023.04.180.
56 N. A. S. Ramli and N. A. S. Amin, *Appl. Catal., B*, 2015, **163**, 487–498, DOI: 10.1016/j.apcatb.2014.08.031.
57 W. H. Knoth and R. L. Harlow, *J. Am. Chem. Soc.*, 1981, **103**, 1865–1867, DOI: 10.1021/ja00397a060.
58 F. Dogan, K. D. Hammond, G. A. Tompsett, H. Huo, W. C. Conner, S. M. Auerbach and C. P. Grey, *J. Am. Chem. Soc.*, 2009, **131**, 11062–11079, DOI: 10.1021/ja9031133.
59 E. F. Freitas, Á. A. L. Araújo, M. F. Paiva, S. C. L. Dias and J. A. Dias, *Mol. Catal.*, 2018, **458**, 152–160, DOI: 10.1016/j.mcat.2018.03.005.
60 H. Fan, J. Su, E. Zhao, Y. Zheng and Z. Chen, *J. Colloid Interface Sci.*, 2025, **684**, 140–147, DOI: 10.1016/j.jcis.2025.01.029.
61 R. Xiao, Z. Luo, Z. Wei, D. Minakata, R. Spinney, S. Wacławek, W. Zeng and C. Tang, *Chin. Chem. Lett.*, 2025, 111853, DOI: 10.1016/j.cclet.2025.111853.
62 C. H. Benison and P. R. Payne, *Curr. Res. Green Sustain. Chem.*, 2022, **5**, 100229, DOI: 10.1016/j.crgsc.2021.100229.
63 Y. Merroun, S. Chehab, A. El Hallaoui, S. Boukhris, R. Ghailane and A. Souizi, *Res. Chem. Intermed.*, 2024, **50**, 3411–3433, DOI: 10.1007/s11164-024-05302-9.